ARMA 24-121

The Energy Budget in Fluid-Driven Fracturing: A Continuum Damage Approach

Mostafa E. Mobasher
Civil and Urban Engineering Department, New York University Abu Dhabi, Abu Dhabi P.O. Box 129188, United Arab Emirates
Haim Waisman
Department of Civil Engineering & Engineering Mechanics, Columbia University, New York, NY 10027

ABSTRACT: We present a numerical approach for the quantification of the energy transfer, storage, and dissipation mechanisms in fluid-driven fracturing. The analysis approach is motivated and originated in the energy statement describing continuum damage, poroelasticity, and the non-local effects in both of damage and transport. The thermodynamically consistent derivation leads to the definition of the state laws, as well the as analytical expressions of energy storage and dissipation in the porous media. The derivation leads to the identification of three major energy loss mechanisms: 1) viscous fluid-flow, 2) solid-damage effect due to the growth of voids and cracks in the solid skeleton, and 3) fluid-damage effect due to the accompanying changes in compressibility and permeability. The analysis model is implemented following the framework of mixed non-linear finite element; and the energy dissipation functions are calculated numerically within this framework. Several benchmark fluid-driven fracturing problems are modeled, and the results agree with the available data from experimental models in the literature. The model is then used to perform several parametric investigations to provide an engineering value of the proposed approach; for example, the analysis of different fluid-injection rates shows most of the additional energy input in higher injection rates is dissipated in viscous fluid flow rather than the sought solid damage. Moreover, the model is used in the analysis of the interaction between fluid-driven fracturing and pre-existing weak zones featuring combinations of reduced stiffness and permeability to represent natural and man-made fractures.

1 INTRODUCTION

Hydraulic fracturing is a process in which a fracturing fluid is pumped at high rates in order to increase the permeability in a fracture zone, ultimately leading to more economical oil production. Energy used in the process is transferred into the porous domain in the form of: (a) elastic energy stored in a deformed domain; (b) energy used to generate new fracture surfaces, resulting in the dissipation of energy through solid skeleton decay (damage); and (c) energy used to transport the fluid through pores, resulting in dissipation via fluid viscosity. The goal of an optimized hydraulic fracturing approach would be to maximize the dissipation due to solid damage, as this would result in the stimulation of a larger reservoir volumeBunger and Lecampion (2017); Shlyapobersky (1985). This paper provides a quantitative evaluation of energy stored and dispersed throughout the process of hydraulic fracturing, based on an non-local damage and transport (NLDT) model modelMobasher et al. (2017); Mobasher (2017); Mobasher et al. (2018); Mobasher and Waisman (2021a,b).

A number of studies have been conducted to calculate the amount of energy storage and energy dissipation in porous media in hydraulic fracturing, including the study in Müller and Sahay (2019) derived energy storage expression for the various categories of Biot's theory. Other exploratory papers, such as the paper by Goodfellow et al. Goodfellow et al. (2015), focused on obtaining experimental insights on hydraulic fracturing energy dissipation. Additionally, numerical modeling approaches

have been used to calculate energy dissipation, such as in Jin et al. (2015); Bunger and Lecampion (2017); Bunger (2013), but these numerical studies are limited to linear elastic fracture mechanics (LEFM) approaches and do not provide an overall continuum description of fracture processes and fluid infiltration into porous media.

The purpose of this paper is to provide a mathematical interpretation and quantification of the energy-dissipation and storage mechanisms of hydraulic fracturing. This paper introduces the mathematical derivation of the dissipation functions emerging from both the solid damage and the fluid viscous flux. The mathematical derivation is based on a thermodynamic free process energy description for the non-local processes in the NLDT model Mobasher and Waisman (2021a). The dissipation functions are quantified within the framework of the implementation of mixed finite elements. This paper is structured as follows: Section 2 provides a description of the energy dissipation model using the state laws derived by the thermodynamic derivative. Section 3 provides a demonstration of the proposed model's capabilities and potential using several benchmark models.

2 ENERGY DISSIPATION AND STORAGE FUNCTIONS

The derivation presented here is an abbreviated version of the full derivation that can be found in Mobasher et al. (2018); Mobasher and Waisman (2021b, 2022). We begin by presenting the Helmholtz free energy expression Ψ^{nl}:

$$\Psi^{nl}(\epsilon_{ij},\tilde{\varepsilon},D,\zeta,\tilde{\zeta}) = \Psi(\epsilon_{ij},\zeta,D)+\Psi^{nl,\varepsilon}(\epsilon_{ij},\tilde{\varepsilon})+\Psi^{nl,\zeta}(\epsilon_{ij},\zeta,\tilde{\zeta}) \tag{1}$$

where $\Psi(\epsilon_{ij},\zeta,D)$, $\Psi^{nl,\varepsilon}$, and $\Psi^{nl,\zeta}$ are the contributions of the stored energy in the poroelastic domain featuring damage, the non-local strain, and the contribution of the non-local transport, respectively. The state variables are the strain ϵ_{ij}, the increment in fluid volume ζ, the damage D, and the non-local variables $\tilde{\varepsilon},\tilde{\zeta}$ which represent non-local strain and non-local fluid volume increment, respectively. Assuming small deformation, the strain can defined as $\epsilon_{ij} = \frac{1}{2}\left[u_{i,j}+u_{j,i}\right]$, where the vector u_i is the solid displacement. Material damage is represented by the phenomenological variable D which varies between 0 for an intact solid and 1 for completely fractured solid.

The solid-damage component Ψ can be decomposed into dry and wet components as Shao (1998):

$$\Psi(\epsilon_{ij},\zeta,D) = \Psi^{dry}(\epsilon_{ij},D)+\Psi^{wet}(\epsilon_{ij},\zeta,D) \tag{2}$$

Ψ^{dry} is the dry component which represents the energy attained by the solid skeleton in undrained conditions ($\zeta = 0$) while, Ψ^{wet}, represents the wet component of the free energy which arises due to the fluid-solid interactions. Hence, they can be defined as:

$$\Psi^{dry}(\epsilon_{ij},D) = \frac{1}{2}C^{u}_{ijkl}(D)\epsilon_{kl}\epsilon_{ij} \tag{3}$$

$$\Psi^{wet}(\epsilon_{ij},\zeta,D) = M(D)\zeta\left[\frac{1}{2}\zeta-\alpha(D)\epsilon_{ii}\right] \tag{4}$$

In the above expressions, $C_{ijkl}(D)$ represents the damage dependent stiffness tensor and the superscript u denotes the undrained conditions. Biot's modulus and coefficient are denoted by M and α, respectively. Their damage-dependent expressions can be found in Mobasher and Waisman (2021a); Shao (1998). The expressions of the energy contributions arising from the non-local variables ($\Psi^{nl,\varepsilon}$) can be found in detail in Mobasher et al. (2018); Peerlings et al. (2004); Polizzotto (2003); Poh and Sun (2017).

In non-local models, the energy dissipation must be defined over the domain as elaborated by Polizzotto (2003). Consequently, the expression for the global dissipation function $\mathcal{D}_t$ can be written as:

$$\mathcal{D}_t = \int_t\int_\Omega \Phi d\Omega dt \tag{5}$$

where Φ is the localization of the global energy dissipation. In other words, Φ is density rate at a material point, and t is time. By decomposing into solid and fluid components, the total energy dissipation can then be rewritten as:

$$\mathcal{D}_t = \mathcal{D}_s+\mathcal{D}_f \geq 0 \tag{6}$$

where $\mathcal{D}_s$ and $\mathcal{D}_s$ are the solid and fluid dissipation components, respectively. Following the definitions in Biot (1972, 1977); Coussy (2004), both terms can be written as:

$$\dot{\mathcal{D}}_s := \int_V \Phi_s dV = \int_V \sigma_{ij}\dot{\epsilon}_{ij}+P\dot{\zeta}-\dot{\Psi}^{nl}dV \geq 0 \tag{7}$$

$$\dot{\mathcal{D}}_f := \int_V \Phi_f dV = \int_V -P_{,i}\,v_i dV \geq 0 \tag{8}$$

where the derivative in time is represented by dot decoration. According to (7), the solid dissipation rate is defined as the difference of the following two factors: (a) the work performed by the first and second terms, which are solid and fluid deformation and flow; and (b) the decay rate of Ψ^{nl}. Equation (8) defines fluid dissipation as the power (rate of work) produced by the fluid velocity v_i on the change in the fluid pressure gradient $P_{,i}$. This definition is consistent with Biot (1972, 1977); Coussy (2004), which describes the energy losses of fluid viscous flow.

The detailed expansion and computation method for the dissipation terms were provided in Mobasher and Waisman (2022).

Overall, the total energy balance in the system has to satisfy:

$$W^{ext} = W^{int} + \mathcal{D}_t \tag{9}$$

where W^{ext} is the external work done at the boundary. A schematic illustrating from Mobasher and Waisman (2022) energy balance is shown in Figure 1. The detailed calculations of internal and external work components W^{int}, W^{ext} were provided in Mobasher and Waisman (2022).

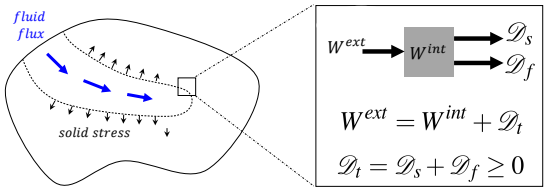

Fig. 1: A schematic from Mobasher and Waisman (2022) illustrating the balance between the external work applied, internal energy stored and dissipated energy.

3 NUMERICAL RESULTS

This section's numerical examples are meant to show how the proposed framework can be used to the numerical quantification of energies that are stored and released during hydraulic fracturing. This is accomplished by modeling a benchmark example of hydraulic fracturing and conducting follow-up studies that quantify the ways in which changes to specific loading, material properties, and modeling setups may result in various energy dissipation methods. The investigations include:

1. hydraulic fracture in materials with varying transport length scales; these varying length scales correspond to varying capillary transport network sizes.
2. varying fluid input rates during hydraulic fracturing

In the following discussions, fracture length L_F, volume V_F and average width w_F are utilized. These parameters are calculated as follows:

- the fractured (damage) volume V_F, which is computed as the domain integral of damage $V_F(t) = \int_V D(t)dV$
- the fracture length $L_F(t)$, which is computed as the distance to the furthest point experiencing damage ($D > 0$) over the center line of the fracture
- the average fracture width $w_F(t)$, which is computed as an approximate value of the fracture volume divided by the fracture length $w_F(t) = \frac{V_F}{L_F}$

3.1. Hydraulic fracturing model

The setup and key findings from the hydraulic fracturing model which will be utilized to calculate energy dissipation are reported in this section. The geometry and material characteristics used in Mobasher and Waisman (2021a) are followed in the model setup. Figure 2, which mimics Figure 6 in Mobasher and Waisman (2021a), depicts a schematic of the boundary conditions, the finite element mesh, and material properties that are identical to those used in Mobasher and Waisman (2022). The time

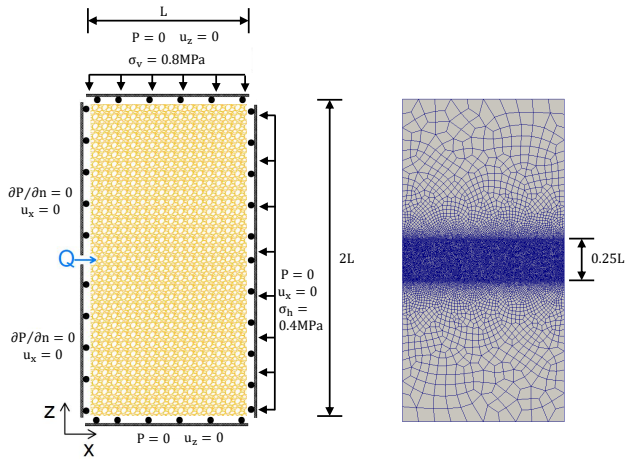

Fig. 2: A schematic showing the boundary conditions and finite element mesh used in the hydraulic fracturing model. Confining stresses of 0.8 MPa (vertical) and 0.4 MPa (horizontal) are applied. This figure resembles Figure 6 in Mobasher and Waisman (2021a).

evolution of internal stored energy, external work done over the poroelastic domain, and energy dissipation are shown in Figure 3. The energy functions in this study were derived and calculated, and the figure indicates that the total of internal energy storage and dissipation equals the external work. Furthermore, the figure illustrates that approximately half of the energy is dissipated and the other half is stored; this finding is consistent with the upper and lower bounds provided in Goodfellow et al. (2015); Boroumand and Eaton (2012).

3.2. Transport length scale variations

We study the effects of using a material with a constant damage length scale but a larger transport length scale on the energy dissipation mechanisms. Larger transport scales are indicative of longer capillary networks and sub-scale networks with wider dispersion in the material Mobasher and Waisman (2021a); Sen and Ramos (2012).

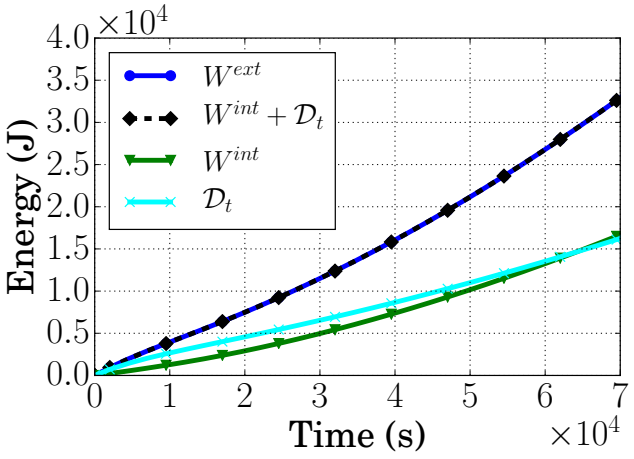

Fig. 3: Evolution of energy storage and dissipation functions. The results are based on the model setup in Section 3.1. The figure was previously published in Mobasher and Waisman (2022).

The non-local damage length scale is maintained constant at $l^D = 0.1$m, but three distinct transport length scales are employed, $l^\kappa = \{0.1, 0.2, 0.5\}$m.

We must first examine how the various transport length scales affect fluid flow and damage distribution before looking into changes to the energy dissipation mechanisms. As a result, we start by charting the damage contours in Figure 4 and the fluid increment ζ contours in Figure 5 along with the fluid flow streamlines. A prior report in Mobasher and Waisman (2021a) examined the impact of a larger transport length scale on the fracture length, width, and volume. Figure 6 displays a portion of the data from Mobasher and Waisman (2021a) for the sake of being comprehensive in this discussion. This comparison revealed that damage zones are bigger and shorter at larger length scales. This observation's initial interpretation might imply that materials with longer length scales could prevent fractures from spreading. On the other hand, Figure 6b research reveals that longer transport length scale material really has a larger damage volume. This discovery indicates that a more diffusive damage process and stimulation over a bigger volume of the poroelastic domain within a less distance from the injection point are caused by higher transport length scales. The findings of the previous studies by Umar et al. (2021); Ratzlaff et al. (2019); Padin et al. (2014); Naik et al. (2019); Bazin et al. (2010) indicate that the presence of microfracture networks and sub-scale fluid networks results in larger Stimulated Reservoir Volumes (SRVs), which are generally supported by the results presented here.

To further our comprehension of the impact of these differ-

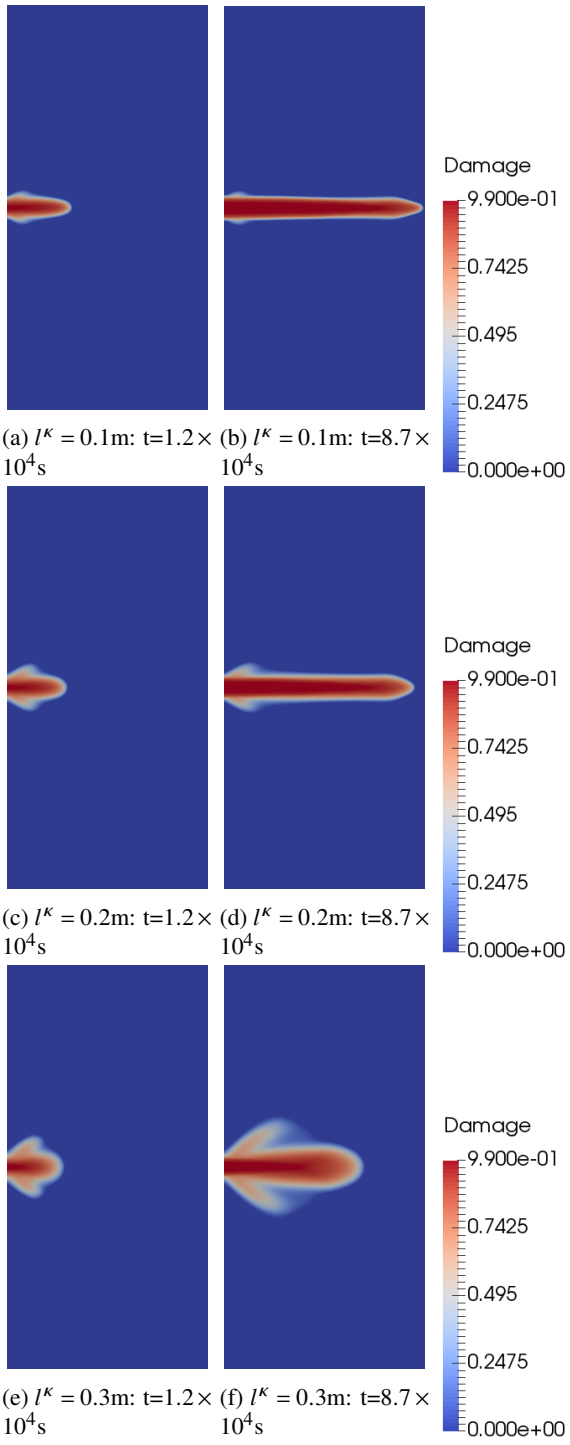

(a) $l^\kappa = 0.1$m: t=1.2$\times 10^4$s (b) $l^\kappa = 0.1$m: t=8.7$\times 10^4$s

(c) $l^\kappa = 0.2$m: t=1.2$\times 10^4$s (d) $l^\kappa = 0.2$m: t=8.7$\times 10^4$s

(e) $l^\kappa = 0.3$m: t=1.2$\times 10^4$s (f) $l^\kappa = 0.3$m: t=8.7$\times 10^4$s

Fig. 4: Evolution of damage contours over time for three different transport length scale values $l^\kappa = \{0.1, 0.2, 0.5\}$m. This figure presents data that is similar to what was previously presented in Mobasher and Waisman (2021a). The figure was previously published in Mobasher and Waisman (2022).

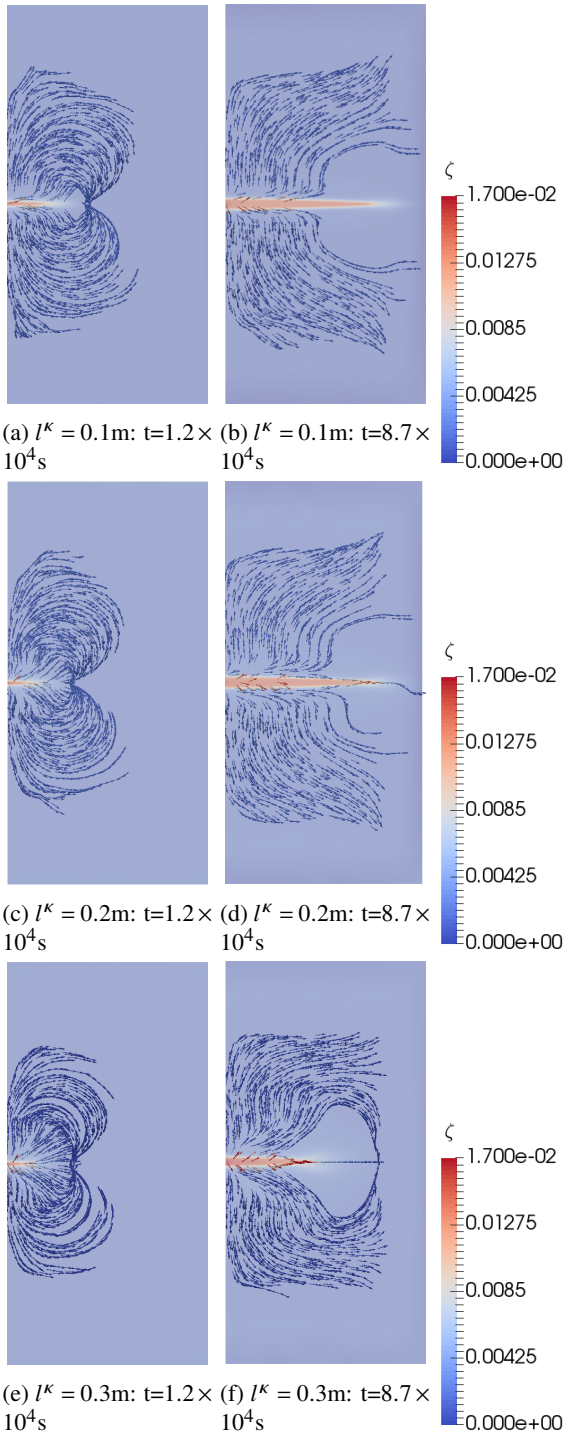

(a) $l^{\kappa} = 0.1$m: t=1.2$\times 10^4$s (b) $l^{\kappa} = 0.1$m: t=8.7$\times 10^4$s

(c) $l^{\kappa} = 0.2$m: t=1.2$\times 10^4$s (d) $l^{\kappa} = 0.2$m: t=8.7$\times 10^4$s

(e) $l^{\kappa} = 0.3$m: t=1.2$\times 10^4$s (f) $l^{\kappa} = 0.3$m: t=8.7$\times 10^4$s

Fig. 5: Evolution of fluid increment ζ over time for three different length scale values $l^{\kappa} = \{0.1, 0.2, 0.5\}$m. The figure was previously published in Mobasher and Waisman (2022).

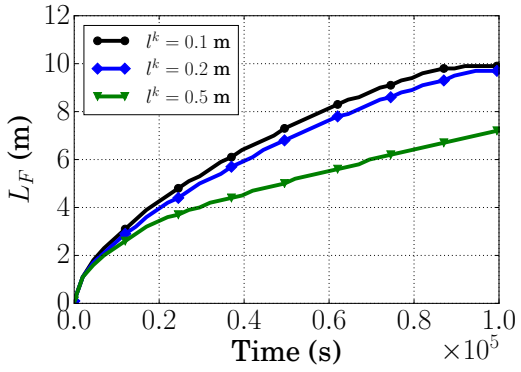

(a) Fracture length L_F

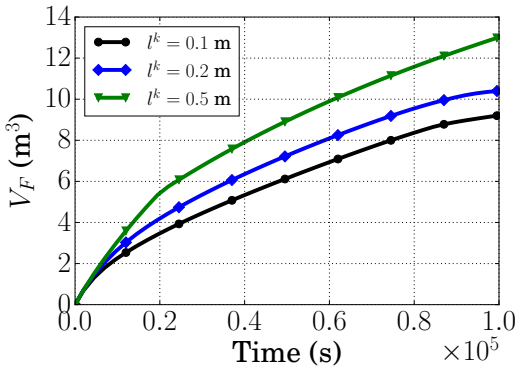

(b) Fracture volume V_F

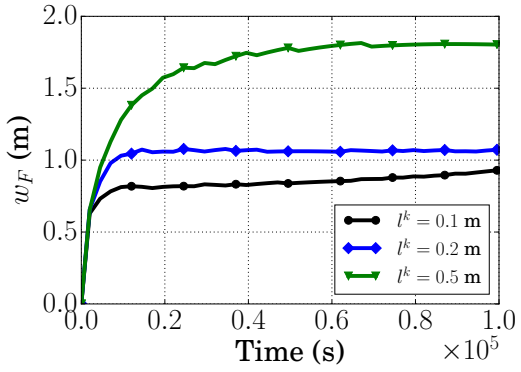

(c) Average fracture width w_F

Fig. 6: The hydraulic driven fracture length, volume and average width evolution against time for different values of transport length scale $l^k = \{0.1, 0.2, 0.5\}$ m. This figure is a partial regeneration of Figure 11 in Mobasher and Waisman (2021a). The figure was previously published in Mobasher and Waisman (2022).

ences in damage zone features on the energy distribution, Figures 7 through 9 illustrate the evolutions of energy dissipation numbers. Figures 7, 8, and 9, respectively, show the energy dissipation evolution in relation to time, fracture length, and fracture volume. Based on general in-

sights, it can be seen that the fluid movement through the porous media dissipates more energy than the processes connected to solid damage.

We can see that the solid dry dissipation and the fluid dissipation are unaffected by the change in the length scale by examining the energy dissipation evolution over time in Figure 7. On the other hand, as the transport length scale increases, the solid wet dissipation decreases. This trend suggests that the wet dissipation is driven by changes in the ratios between the solid and fluid compressibilities, and that these changes are significantly impacted by greater transport length scales. Nevertheless, a distinct perspective emerges from a closer examination of the dissipation functions evolution throughout the fracture length and volume in Figures 8 and 9. While the final values of dissipated energy are the same for all length scales, the solid dissipation rate with respect to fracture length increases as the length scale increases (see Figure 8a), while the solid dissipation rate with respect to fracture volume decreases as the length scale increases (see Figure 9a). According to these results, materials with longer length scales should be predicted to release more energy during the development of damage per unit length of the fracture; in other words, in this instance, fluid dissipation through subscale networks is facilitating the formation of the fracture.

Conversely, as can be shown in Figure 8b, the solid wet dissipation rate per fracture volume falls with increasing length scales, whereas the solid wet dissipation rate versus fracture length remains constant throughout length scales. Based on the solid wet dissipation trends observed, materials with longer transport length scales will exhibit less overall dissipation due to a decrease in the volume of the fracture and the amount of solid wet dissipation with time. These findings could also be used to sway the decision regarding the compressibility of the fracking fluid Wang et al. (2018); Park and Kim (2016). While the rate with respect to fracture volume 9c shows the opposite trend, the examination of the fluid dissipation rate with regard to fracture length 8c demonstrates a rising rate as the length scale increases. The longer length scales nevertheless result in an overall higher fluid dissipation per length of the fracture, but this behavior can be explained by the decreased localization in the larger length scales, which leads to smaller fluid velocities per material point and hence lower dissipation per volume.

A greater understanding of the energy dissipation during fracking through materials with wider sub-scale networks can be gained from the observations based on the analysis presented in this section, both qualitatively and quantitatively Cui and Han (2018). The materials with longer transport length scales that these geomaterials possess are showcased here.

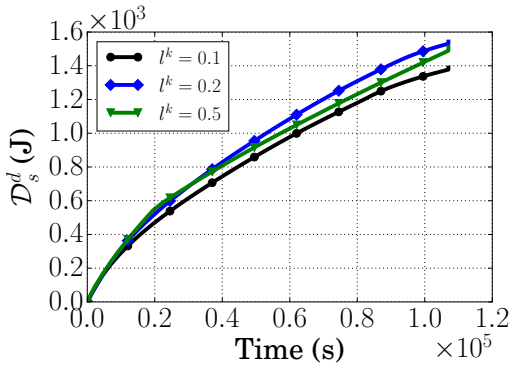

(a) Dry solid dissipation

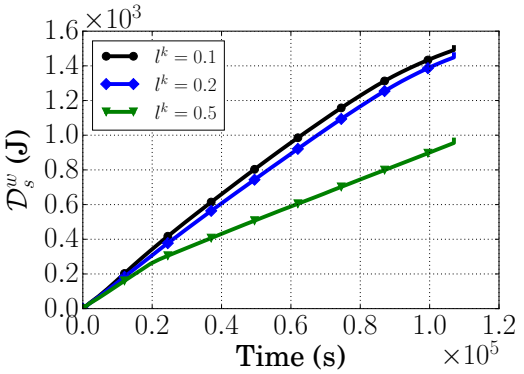

(b) Wet solid dissipation

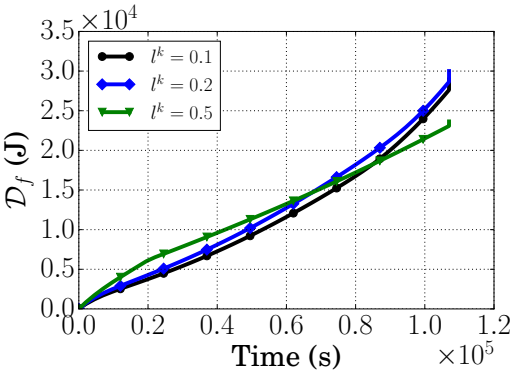

(c) Fluid dissipation

Fig. 7: The influence of various transport length scales on the energy dissipation over time. The figure was previously published in Mobasher and Waisman (2022).

3.3. Fluid injection rate variations

We examine the impact of higher fluid injection rates on the fluid-driven fracture propagation in this section. Using $l^D = l^\kappa = 0.1$m, we try three alternative injection rates in these simulations: $Q, 2Q, 3Q$. Hydraulic fracturing

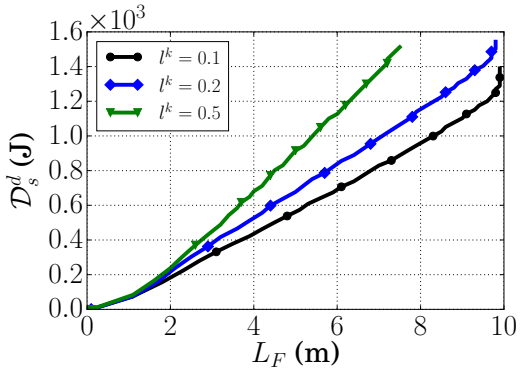

(a) Dry solid dissipation

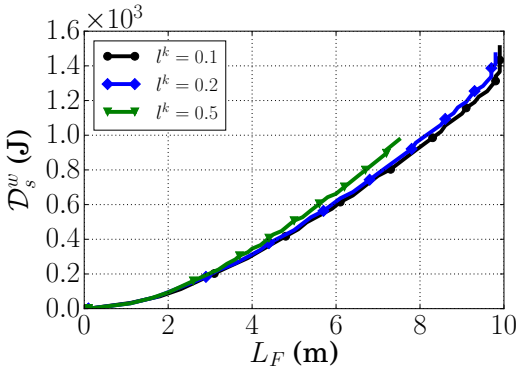

(b) Wet solid dissipation

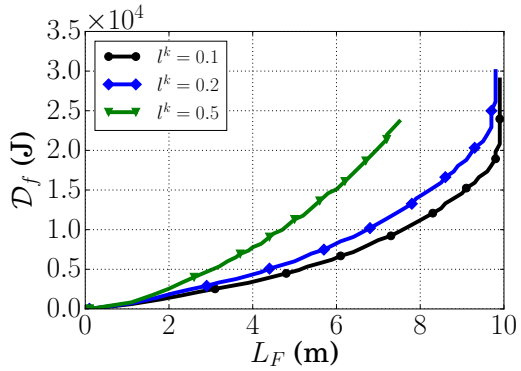

(c) Fluid dissipation

Fig. 8: The influence of various transport length scales on the energy dissipation over fracture length. The figure was previously published in Mobasher and Waisman (2022).

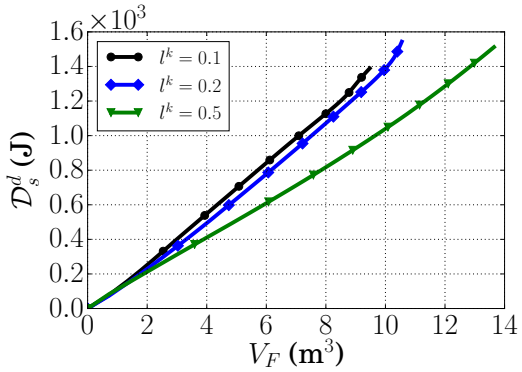

(a) Dry solid dissipation

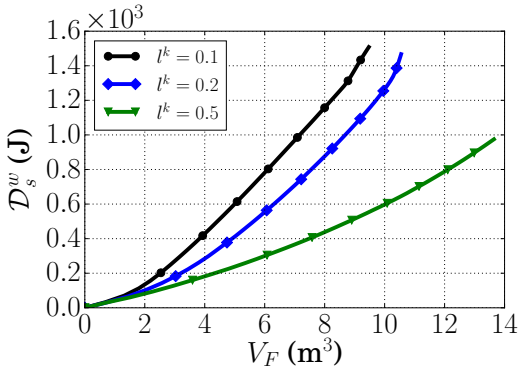

(b) Wet solid dissipation

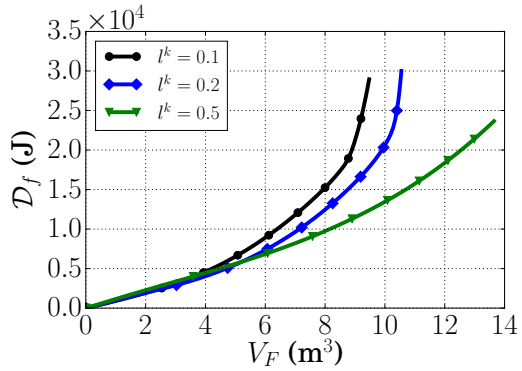

(c) Fluid dissipation

Fig. 9: The influence of various transport length scales on the energy dissipation fracture volume. The figure was previously published in Mobasher and Waisman (2022).

costs have a direct association with fluid injection rates since greater pumping rates are more expensive Fitzgerald (2012); Starovoitova et al. (2018). Thus, it would be helpful to know if pumping more fluid will result in greater damage quantities over shorter times.

Figures 10 and 11, respectively, display the damage and fluid increment ζ contours for the $2Q$ and $3Q$ injection rates. Figures 4a, 4b, 5a, and 5b all display contours for the Q injection rate that are similar to this one. Furthermore, the progression of fracture length, width, and volume over time is shown in Figure 12. The findings indicate that slightly smaller damage bands are produced by higher injection rates. This can be explained by the fact that higher pumping rates will put greater pressure on the localized damage front, which will cause the fracture to

propagate more locally and less diffusely. The findings tally with earlier findings documented in Lin et al. (2017); Wasantha et al. (2021); Fallahzadeh et al. (2015).

Higher injection rates have been demonstrated to cause fractures to propagate more quickly. Nevertheless, the examination of Figures 10 through 12 does not provide us with enough details regarding the proportion of extra energy consumed at higher pumping rates that is truly utilized to propagate damage. Consequently, we exhibit the evolution amounts of energy dissipation for each of the three pumping rates in Figures 13 through 15. Figures 13, 14, and 15, respectively, show the energy dissipation evolution with regard to time, fracture length, and fracture volume. These findings allow for the generalization of two conclusions. First, in accordance with the findings in this Section, the fluid damage dissipation is greater than the solid damage dissipation. The second is that, although there are additional observations that are outlined below, the energy dissipation rate increases as the pumping rate increases.

As shown in Figure 13, we plot the dissipation evolution with time. Apart from the increased rate of dissipation in relation to time, there is also a larger value of accumulated dissipation for both solid dry and fluid dissipation. While all models achieve about the same total cumulative energy dissipation, this is not the case for the solid wet dissipation, which shows a higher dissipation rate with faster injection. These results suggest that increased damage and permeability growth are directly caused by faster fluid injection, and that this increases total accumulated solid dry and fluid dissipation. On the other hand, only the evolution rate, not the total accumulated value, is impacted by changes in the relative compressibilities of the fluid and solid constituents, which results in the dissipation of energy. The results in Figures 14 and 15 help to clarify these conclusions. Regarding fracture length and volume, the solid wet dissipation evolution rate is nearly independent of the injection rate. In the meantime, it is evident that higher injection rates result in greater solid dry and fluid dissipation per unit length and volume.

The results presented in this section show that injecting fluid at higher rates will directly increase the rate and total amounts of energy dissipation within the ratios examined in this study. This is often a desirable result, and fracking can be accelerated by raising the injection rate Rahman et al. (2003); Zhuang et al. (2019); Morgan et al. (2017).

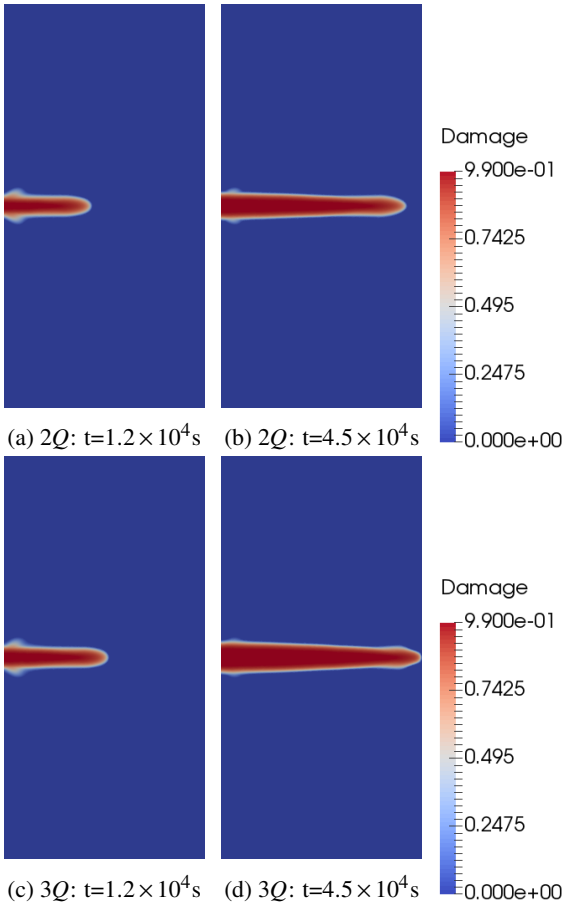

Fig. 10: Evolution of damage contours over time for different transport length scale values $2Q$ and $3Q$. The damage case for the Q injection rate case is shown in Figure 4. The figure was previously published in Mobasher and Waisman (2022).

4 SUMMARY AND CONCLUSION

In this work, we provide a sound method for calculating the energy dissipation that occurs in porous media

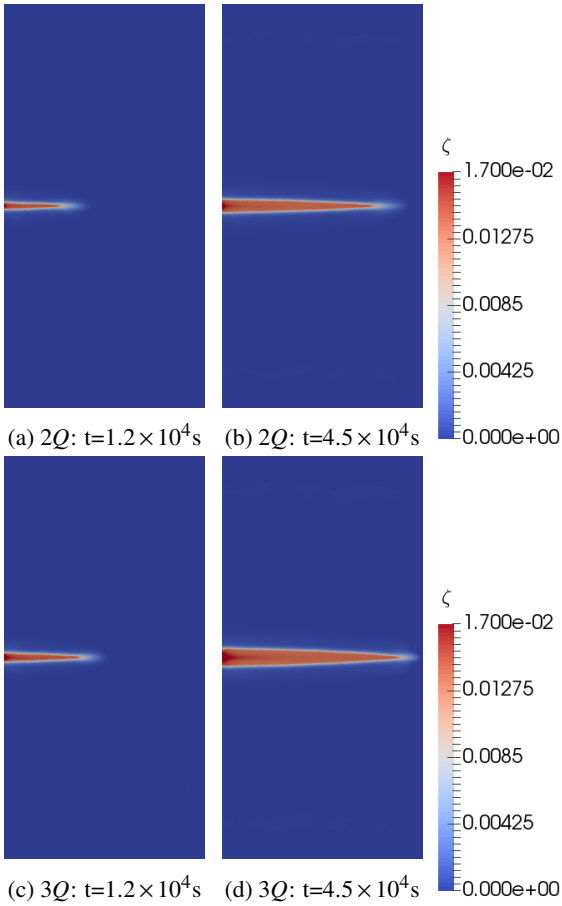

(a) $2Q$: t=1.2×10^4s (b) $2Q$: t=4.5×10^4s

(c) $3Q$: t=1.2×10^4s (d) $3Q$: t=4.5×10^4s

Fig. 11: Evolution of fluid increment ζ contours over time for different transport length scale values $2Q$ and $3Q$. The damage case for the Q injection rate case is shown in Figure 5. The figure was previously published in Mobasher and Waisman (2022).

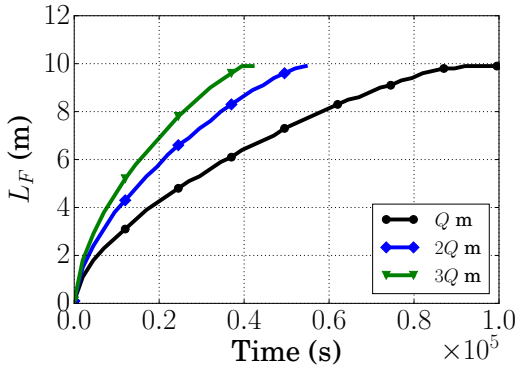

(a) Fracture length L_F

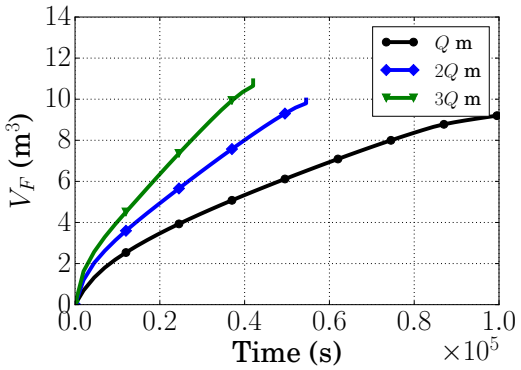

(b) Fracture volume V_F

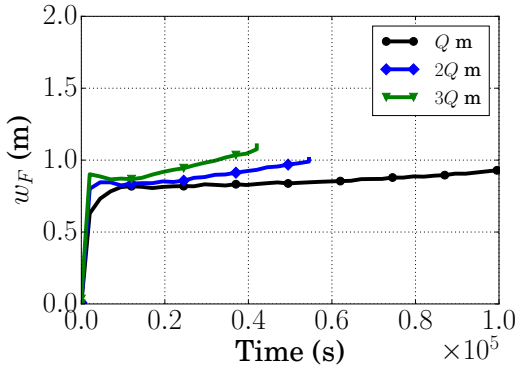

(c) Average fracture width w_F

Fig. 12: The hydraulic driven fracture length , volume and average width evolution against time for different values of input fluid flux $Q, 2Q, 3Q$. The figure was previously published in Mobasher and Waisman (2022).

when fluid flow and damage propagation are combined. The non-local damage transport (NLDT) model, which is based on thermodynamics principles, serves as the foundation for the energy dissipation functions. Several parametric investigations are conducted to examine the effects of different material qualities and loading circumstances on energy dissipation mechanisms and overall fracture

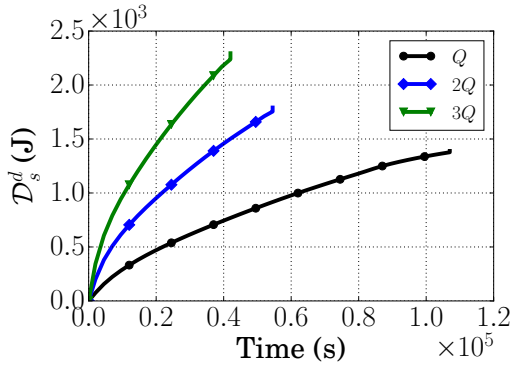

(a) Solid dry dissipation

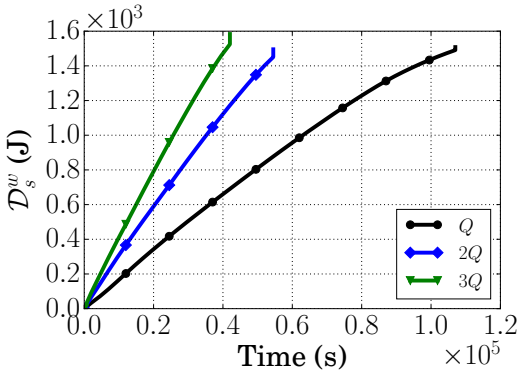

(b) Solid wet dissipation

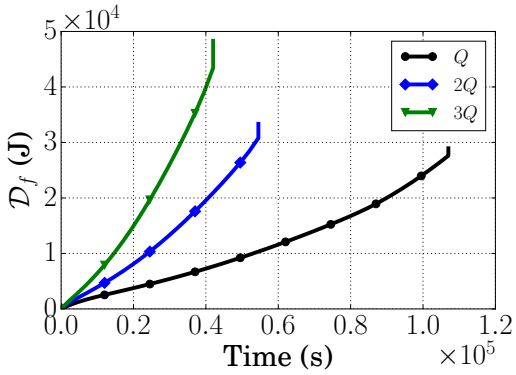

(c) Fluid dissipation

Fig. 13: Influence of the variation of injection rates on the damage dissipation over time. The figure was previously published in Mobasher and Waisman (2022).

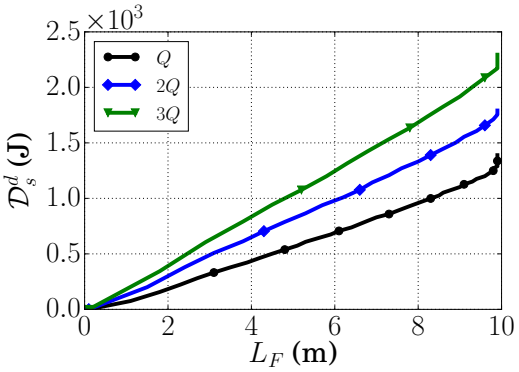

(a) Solid dry dissipation

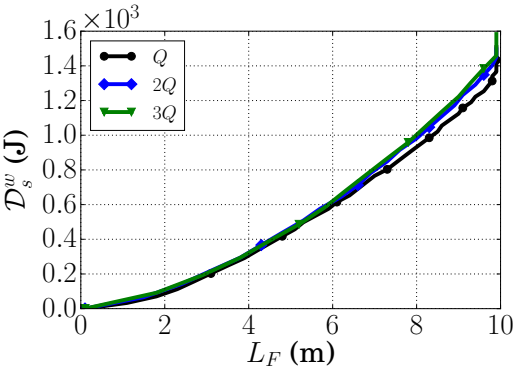

(b) Fluid dissipation

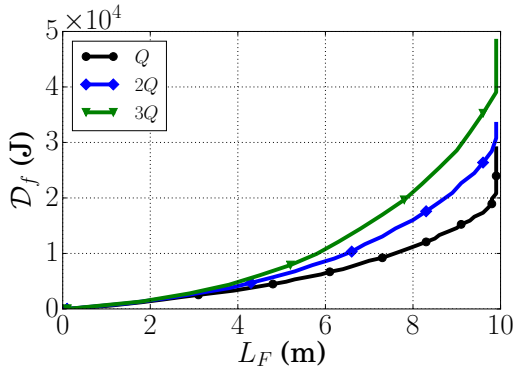

(c)

Fig. 14: Influence of the variation of injection rates on the damage dissipation over fracture length. The figure was previously published in Mobasher and Waisman (2022).

propagation. The model is used to a benchmark hydraulic fracturing case.

The energy dissipation in geomaterials with wider subscale capillary networks can be better understood by varying the non-local length scale. The available field observations and experimental data are consistent with the fluid injection rate variation, which indicates that an increase in pumping rate causes a corresponding increase in fracture length and volume. The resulting evolution in permeability and damage governs the energy dissipation under higher injection rates. The presented model can be further capitalized on as basis for hydraulic fracturing optimization that is informed by the energy dissipation mechanisms.

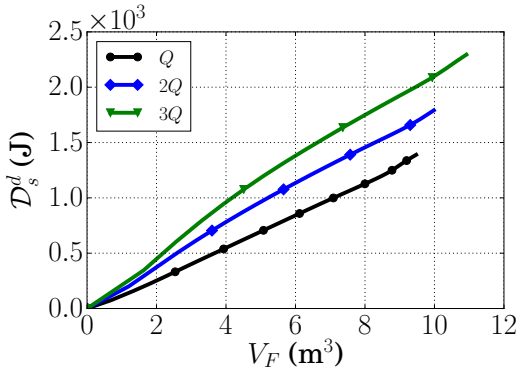

(a) Solid dry dissipation

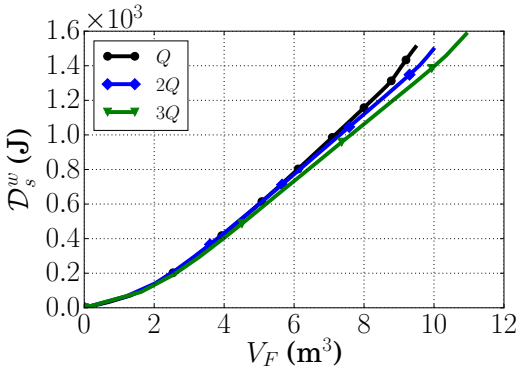

(b) Solid wet dissipation

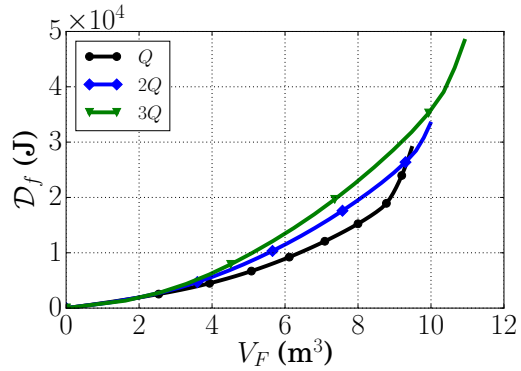

(c) Fluid dissipation

Fig. 15: Influence of the variation of injection rates on the damage dissipation over fracture volume. The figure was previously published in Mobasher and Waisman (2022).

ACKNOWLEDGMENT

This work was partially supported by the Sand Hazards and Opportunities for Resilience, Energy, and Sustainability (SHORES) Center, funded by Tamkeen under the NYUAD Research Institute Award CG013.

REFERENCES

1. Bazin, B., Peysson, Y., Lamy, F., Martin, F., Aubry, E., and Chapuis, C. (2010). In-situ water-blocking measurements and interpretation related to fracturing operations in tight gas reservoirs. *SPE Production & Operations*, 25(04):431–437.

2. Biot, M. A. (1972). Theory of finite deformations of porous solids. *Indiana University Mathematics Journal*, 21(7):597–620.

3. Biot, M. A. (1977). Variational lagrangian-thermodynamics of nonisothermal finite strain mechanics of porous solids and thermomolecular diffusion. *International Journal of Solids and Structures*, 13(6):579–597.

4. Boroumand, N. and Eaton, D. W. (2012). Comparing energy calculations-hydraulic fracturing and microseismic monitoring. In *74th EAGE Conference and Exhibition incorporating EUROPEC 2012*, pages cp–293. European Association of Geoscientists & Engineers.

5. Bunger, A. (2013). Analysis of the power input needed to propagate multiple hydraulic fractures. *International Journal of Solids and Structures*, 50(10):1538–1549.

6. Bunger, A. and Lecampion, B. (2017). Four critical issues for successful hydraulic fracturing applications. *Rock mechanics and engineering*, (BOOK_CHAP).

7. Coussy, O. (2004). *Poromechanics*. John Wiley & Sons.

8. Cui, Z. and Han, W. (2018). In situ scanning electron microscope (sem) observations of damage and crack growth of shale. *Microscopy and Microanalysis*, 24(2):107.

9. Fallahzadeh, S., James Cornwell, A., Rasouli, V., and Hossain, M. (2015). The impacts of fracturing fluid viscosity and injection rate on the near wellbore hydraulic fracture propagation in cased perforated wellbores. In *49th US Rock Mechanics/Geomechanics Symposium*. OnePetro.

10. Fitzgerald, T. (2012). Frackonomics: some economics of hydraulic fracturing. *Case W. Res. L. Rev.*, 63:1337.

11. Goodfellow, S., Nasseri, M., Maxwell, S., and Young, R. (2015). Hydraulic fracture energy budget: Insights from the laboratory. *Geophysical Research Letters*, 42(9):3179–3187.

12. Jin, W., Xu, H., and Arson, C. (2015). Energy dissipation during mode i fracture propagation in shale: Comparison between a continuum damage model, a cohesive zone model and the extened finite element method. In *13th ISRM International Congress of Rock Mechanics*. OnePetro.

13. Lin, C., He, J., Li, X., Wan, X., and Zheng, B. (2017). An experimental investigation into the effects of the anisotropy of shale on hydraulic fracture propagation. *Rock Mechanics and Rock Engineering*, 50(3):543–554.

14. Mobasher, M. (2017). *Enhanced continuum damage modeling of mechanical failure in ice and rocks*. PhD thesis, Columbia University.

15. Mobasher, M. E., Berger-Vergiat, L., and Waisman, H. (2017). Non-local formulation for transport and damage in porous media. *Computer Methods in Applied Mechanics and Engineering*, 324:654–688.

16. Mobasher, M. E. and Waisman, H. (2021a). Dual length scale non-local model to represent damage and transport in porous media. *Computer Methods in Applied Mechanics and Engineering*, 387:114154.

17. Mobasher, M. E. and Waisman, H. (2021b). Non-local continuum damage and transport modeling framework for hydraulic fracturing. In *ARMA/DGS/SEG 2nd International Geomechanics Symposium*. OnePetro.

18. Mobasher, M. E. and Waisman, H. (2022). Energy dissipation mechanisms in fluid driven fracturing of porous media. *Geomechanics and Geophysics for Geo-Energy and Geo-Resources*, 8(5):157.

19. Mobasher, M. E., Waisman, H., and Berger-Vergiat, L. (2018). Thermodynamic framework for non-local transport-damage modeling of fluid driven fracture in porous media. *International Journal of Rock Mechanics and Mining Sciences*, 111:64–83.

20. Morgan, S., Li, B., and Einstein, H. (2017). Effect of injection rate on hydraulic fracturing of opalinus clay shale. In *51st US Rock Mechanics/Geomechanics Symposium*. OnePetro.

21. Müller, T. M. and Sahay, P. N. (2019). Elastic potential energy in linear poroelasticity. *Geophysics*, 84(4):W1–W20.

22. Naik, S., Yang, S., Woolley, M., and Bedrikovetsky, P. (2019). Analytical modelling of the water block phenomenon in hydraulically fractured wells. *Journal of Natural Gas Science and Engineering*, 67:56–70.

23. Padin, A., Tutuncu, A. N., and Sonnenberg, S. (2014). On the mechanisms of shale microfracture propagation. In *SPE Hydraulic Fracturing Technology Conference*. OnePetro.

24. Park, J. and Kim, J. (2016). Importance of fluid compressibility and multi-phase flow in numerical modeling of hydraulic fracture propagation. In *50th US Rock Mechanics/Geomechanics Symposium*. OnePetro.

25. Peerlings, R., Massart, T., and Geers, M. (2004). A thermodynamically motivated implicit gradient damage framework and its application to brick masonry cracking. *Computer methods in applied mechanics and engineering*, 193(30):3403–3417.

26. Poh, L. H. and Sun, G. (2017). Localizing gradient damage model with decreasing interactions. *International Journal for Numerical Methods in Engineering*, 110(6):503–522.

27. Polizzotto, C. (2003). Unified thermodynamic framework for nonlocal/gradient continuum theories. *European Journal of Mechanics-A/Solids*, 22(5):651–668.

28. Rahman, M., Rahman, M., and Rahman, S. (2003). Optimizing treatment parameters for enhanced hydrocarbon production by hydraulic fracturing. *Journal of Canadian Petroleum Technology*, 42(06).

29. Ratzlaff, C., Sondergeld, C., Rai, C., Curtis, M., and Jernigen, J. (2019). Sem investigation of the fracture network (stimulated reservoir volume) induced by hydraulic fracturing in tennessee sandstone. In *53rd US Rock Mechanics/Geomechanics Symposium*. OnePetro.

30. Sen, M. and Ramos, E. (2012). A spatially non-local model for flow in porous media. *Transport in Porous Media*, 92(1):29–39.

31. Shao, J. (1998). Poroelastic behaviour of brittle rock materials with anisotropic damage. *Mechanics of Materials*, 30(1):41–53.

32. Shlyapobersky, J. (1985). Energy analysis of hydraulic fracturing. In *The 26th US Symposium on Rock Mechanics (USRMS)*. OnePetro.

33. Starovoitova, B., Golovin, S., Paderin, G., Shel, E., Kavunnikova, E., and Krivtsov, A. (2018). Design optimization of hydraulic fracturing. In *IOP Conference Series: Earth and Environmental Science*, volume 193, page 012011. IOP Publishing.

34. Umar, I. A., Negash, B. M., Quainoo, A. K., and Ayoub, M. A. (2021). An outlook into recent advances on estimation of effective stimulated reservoir volume. *Journal of Natural Gas Science and Engineering*, 88:103822.

35. Wang, D., Chen, M., Jin, Y., Bunger, A., et al. (2018). Effect of fluid compressibility on toughness-dominated hydraulic fractures with leakoff. *SPE Journal*, 23(06):2118–2132.

36. Wasantha, P., Xu, T., and Xu, B. (2021). Effect of fluid injection rate on the hydraulic fracture propagation characteristics. In *IOP Conference Series: Earth and Environmental Science*, volume 861, page 032095. IOP Publishing.

37. Zhuang, L., Kim, K. Y., Jung, S. G., Diaz, M., and Min, K.-B. (2019). Effect of water infiltration, injection rate and anisotropy on hydraulic fracturing behavior of granite. *Rock Mechanics and Rock Engineering*, 52(2):575–589.